nature communications

Article

https://doi.org/10.1038/s41467-025-61656-7

Chromatin interaction maps of human arterioles reveal mechanisms for the genetic regulation of blood pressure

Received: 23 October 2024

Accepted: 24 June 2025

Published online: 17 July 2025

Check for updates

Yong Liu[1,2,9], Rajan Pandey[1,2,9], Qiongzi Qiu[1,2,9], Pengyuan Liu[1,2,9], Hong Xue[3,9], Jingli Wang[4], Bhavika Therani[1,2], Rong Ying[4], Kristie Usa[3], Michael Grzybowski[3], Chun Yang[3], Manoj K. Mishra[1,2], Andrew S. Greene[5], Allen W. Cowley Jr.[3], Sridhar Rao[6,7,8], Aron M. Geurts[3], Michael E. Widlansky[4] & Mingyu Liang[1,2]

Arterioles are small blood vessels located just upstream of capillaries in nearly all tissues. Despite the broad and essential role of arterioles in physiology and disease, current knowledge of the functional genomics of arterioles is largely absent. Here, we report extensive maps of chromatin interactions, single-cell expression, and other molecular features in human arterioles and uncover mechanisms linking human genetic variants to gene expression in vascular cells and the development of hypertension. Compared to large arteries, arterioles exhibited a higher proportion of pericytes which were enriched for blood pressure (BP)-associated genes. BP-associated single nucleotide polymorphisms (SNPs) were enriched in chromatin interaction regions in arterioles. We linked BP-associated noncoding SNP rs1882961 to gene expression through long-range chromatin contacts and revealed remarkable effects of a 4-bp noncoding genomic segment on hypertension in vivo. We anticipate that our data and findings will advance the study of the numerous diseases involving arterioles.

Arterioles are small blood vessels found just upstream of capillary beds in nearly all tissues[1–3]. Arterioles have diameters of 10 to 300 μm and consist of one layer of endothelial cells (EC) and one to a few layers of smooth muscle cells. The constriction and dilation of arterioles controls the blood flow to tissue regions. Therefore, arteriolar function is essential for maintaining proper distribution of blood across tissue regions at rest and changing blood flow in response to stimuli such as stress, exercise, and food ingestion[1–3]. Additionally, arterioles are critical for determining systemic blood pressure (BP). BP is the product of total peripheral vascular resistance and cardiac output. Arterioles account for 60% to 70% of total peripheral vascular resistance in humans. Abnormalities in arterioles contribute to the development of major diseases such as hypertension, stroke, and many other microvascular complications of diabetes and hypertension[4–6].

Despite the broad and essential role of arterioles in physiology and disease, current knowledge of the functional genomic features of arterioles is limited. This is in part because it is difficult to obtain arteriole samples for analysis, which requires skilled, microscopic tissue dissection[5]. Some functional genomic data is available for larger arteries with diameters of several mm or more. For example, the

[1]Department of Physiology, University of Arizona College of Medicine—Tucson, Tucson, AZ, USA. [2]Molecular Systems Medicine Initiative, University of Arizona Health Sciences, Tucson, AZ, USA. [3]Department of Physiology, Medical College of Wisconsin, Milwaukee, WI, USA. [4]Cardiovascular Center and Department of Medicine, Medical College of Wisconsin, Milwaukee, WI, USA. [5]The Jackson Laboratory, Bar Harbor, ME, USA. [6]Versiti Blood Research Institute, Milwaukee, WI, USA. [7]Department of Pediatrics, Division of Hematology, Oncology, and Transplantation, Medical College of Wisconsin, Milwaukee, WI, USA. [8]Department of Cell Biology, Neurobiology, and Anatomy, Medical College of Wisconsin, Milwaukee, WI, USA. [9]These authors contributed equally: Yong Liu, Rajan Pandey, Qiongzi Qiu, Pengyuan Liu, Hong Xue. e-mail: mliang1@arizona.edu

Encyclopedia of DNA Elements (ENCODE) project and the Genotype-Tissue Expression (GTEx) project include aorta, coronary artery, and tibial artery in their analysis[7,8]. However, larger arteries and arterioles are structurally and physiologically highly distinct. Larger arteries do not contribute to the regulation of tissue perfusion or BP as arterioles do, and they contained more layers of smooth muscle cells and more elastic tissues than arterioles[9,10]. Therefore, functional genomic insights obtained from the analysis of larger arteries may not be applicable to arterioles, leaving a critical knowledge gap.

In this study, we established an extensive epigenomic landscape for human arterioles. We generated data for global and promoter-focused chromatin conformation, DNA methylation, and bulk and single-nucleus gene expression in human arterioles or tissue components of human arterioles. We carried out integrated analysis of these datasets with single nucleotide polymorphisms (SNPs) associated with vascular traits including BP identified by previous genome-wide association studies (GWAS). We further investigated the BP-associated, noncoding SNP rs1882961 that we found to form long-range chromatin interactions with *NRIP1* promoter. Using genome editing in animal models and human induced pluripotent stem cells (hiPSCs), we uncovered the mechanism by which rs1882961 regulated *NRIP1* expression and demonstrated robust effects for a rs1882961 orthologous site on BP in a rat model.

Results

The cellular composition and properties of human arterioles are distinct from larger arteries

We started by examining the cell type composition of human arterioles using single-nucleus RNA-seq (snRNA-seq). The arterioles were dissected from adipose tissues from surgical discards. Three arterioles, one from each subject, were pooled to provide sufficient material for snRNA-seq (Supplementary Data S1). The arterioles were 100-150 µm in diameter and a few mm long.

Despite the small amount of input tissue, we obtained snRNA-seq data meeting our quality criteria from 1205 nuclei. We detected several major cell types previously detected in the thoracic aorta using the same set of marker genes[11] (Fig. 1A, B). The proportions of the cell types were substantially different between the arteriole and the aorta. To account for variable recovery rates for different cell types during nucleus isolation, we calculated proportions of cell types relative to EC in each tissue. The proportion of pericytes was higher in arterioles than in aorta (ratio = 1.31 in arterioles vs. 0.65 in aorta), whereas the proportion of vascular smooth muscle cells was lower in arterioles (ratio = 0.22 in arterioles vs. 11.19 in aorta) (Fig. 1C). For each cell type, the Spearman correlation coefficients of gene expression profiles between the arteriole and the aorta ranged from 0.52 to 0.76 (Fig. 1D). We examined the enrichment of genes reported by genome-wide association studies (GWAS) of arteriole-related traits in each cell type. GWAS for diastolic BP, systolic BP, pulse pressure, hypertension, stroke, diabetic nephropathy, diabetic retinopathy, and peripheral arterial disease were included in this analysis. We found that BP-associated GWAS genes were enriched in several arteriolar and aorta cell types but to substantially different extents (Fig. 1E). Genes associated with diastolic BP were enriched in arteriolar, but not aortic, endothelial cells, and they were substantially more enriched in arteriolar pericytes ($\beta = 0.35$) than aortic pericytes ($\beta = 0.11$). Genes associated with systolic BP and pulse pressure were enriched in aortic, but not arteriolar, smooth muscle cells and in arteriolar fibroblasts ($\beta = 0.14$ and 0.32, respectively) much more than aortic fibroblasts ($\beta = 0.09$ and 0.1) (Fig. 1E).

Chromatin interactions, transcriptome, and DNA methylation in human arterioles

We constructed reference profiles of chromatin interactions, gene expression, and DNA methylation in human arterioles. The source subjects included a mix of race and sex (Supplementary Data S1). From each subject, one or more arterioles were separated into endothelial cells and endothelium-denuded arterioles (EDA), and one or more were analyzed as intact arterioles without the separation. The chromatin interaction analysis required more input material than what was available from a single subject. Therefore, arteriolar tissues from several subjects were combined to generate a reference chromatin interaction map for each tissue component.

Two chromatin interaction assays were performed: a Micro-C assay for global mapping and a pan-promoter capture Micro-C assay for mapping chromatin interactions with promoters of more than 27,000 coding and noncoding genes.

The Micro-C assay generated 315 million and 406 million unique read pairs in intact arterioles and EDA, respectively, resulting in the detection of an average of 1,037, 4,156, and 4,946 chromatin loops at 4-kbp, 8-kbp, and 16-kbp resolution, respectively (Supplementary Datas S2–S9). All loops were intrachromosomal by the default settings of the analysis. The median loop size ranges from 96 kbp at 4-kbp resolution to nearly 500 kbp at 16-kbp resolution (Supplementary Fig. S1). It is likely that we only detected a portion of the loops in each tissue type because of the sequencing depth and the low amounts of input material limiting the library complexity. Despite this limitation, significant overlaps, defined as overlap of both contact regions that defined a loop, were observed between loops detected in the two tissue types (Fig. 2A). For example, at the 16 kbp resolution, 33% of all detected loops were shared between intact arterioles and EDAs (Fig. 2A). Only a few dozen loops were detected in arteriolar endothelial cells, suggesting that, even with pooling, the amount of material in the arteriolar endothelial cell sample was insufficient for detecting most chromatin loops.

The pan-promoter capture Micro-C assay detected more than 100,000 and 80,000 chromatin interactions with promoters at 10-kbp and 20-kbp resolution, respectively, in intact arterioles and EDAs (Supplementary Datas S2, S10–S14). 60% to 73% of these contacts were intrachromosomal. On average, 48,220 intrachromosomal promoter interactions with distances between chromatin contacts from 10 kbp to 2 million bp were included in the downstream analysis. Chromatin interactions were detected for the promoters of 4,595 to 10,443 of the 20,089 protein-coding genes covered by the human pan-promoter probe panel in intact Arterioles and EDAs at 10-kbp or 20-kbp resolution. The median distance of the interacting regions was 102.1 kbp to 112.4kbp (Supplementary Fig. S2). Substantial overlaps, defined by overlap of both contact regions, were observed between interactions detected in the two tissue types. At 10- and 20-kbp resolution, 26% to 34% of the interactions were shared between intact arterioles and EDAs (Fig. 2B). More interactions were detected at 1-, 2-, or 5-kbp resolution, but the percent of intrachromosomal interactions were below 35% and the overlaps between the two tissues were less than 2%, suggesting greater noise in the result at these resolutions. No significant interactions were detected in the arteriolar endothelia sample likely because of, again, insufficient input material.

Poly(A)-dependent bulk RNA-seq analysis ($n = 3$ each) (Supplementary Datas S2, Fig. S3) indicated that, as expected, the transcriptome profiles of arteriolar endothelial cells differed substantially from the intact arterioles and EDAs, with 2891 and 2939 differentially expressed genes (FDR < 0.05), respectively (Supplementary Fig. S3). The arteriolar endothelial cells were enriched for endothelial marker genes, while the arterioles and EDAs were enriched for marker genes for vascular smooth muscles (Supplementary Fig. S4). 754 genes were differentially expressed between arterioles and EDAs (FDR < 0.05).

Reduced representation bisulfite sequencing (RRBS) (Supplementary Data S2) identified only a few differentially

https://doi.org/10.1038/s41467-025-61656-7

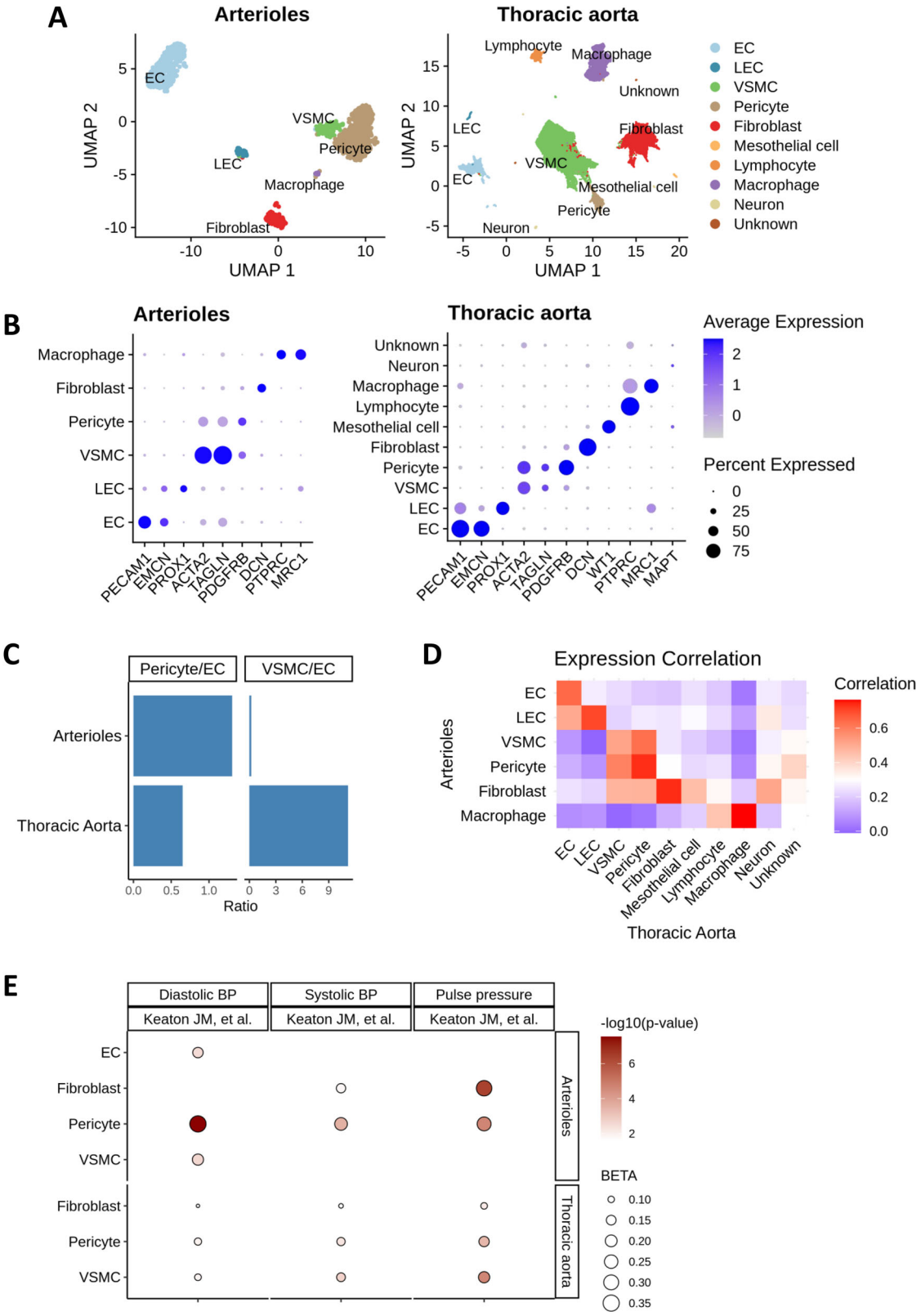

methylated regions (DMRs; FDR < 0.05) between arteriolar endothelial cells and either intact arterioles (1 DMR) or EDAs (25 DMRs). No DMRs were observed between EDAs and intact arterioles. These small differences may be attributed to the limited sample size. Similar to previous reports[12,13], the overall correlation between RNA abundance and gene promoter methylation was limited (Supplementary Fig. S5).

Chromatin contact regions are enriched for regulatory elements and associated with higher gene expression

We obtained DNA regulatory elements including enhancers, promoters, and transcriptional factor binding sites from Ensembl[14]. These regulatory elements were defined as genomic regions with biochemical activity, identified through a four-step Regulatory Build process[15], which integrated all available epigenomic data from the ENCODE and

Fig. 1 | The cellular composition and properties of human arterioles exhibit distinct features compared with the aorta. A UMAP plot showing major cell types identified in arteriole (this study) and thoracic aorta (Pirruccello, J.P. et al., 2022) snRNA-seq data. **B** Dot plot displaying expression of conventional marker gene across cell types. Dot size represents the percentage of cells expressing each gene, and color intensity indicates the average expression level. **C** Relative proportions of pericytes to ECs and VSMCs to ECs in arteriole and thoracic aorta, shown separately. **D** Heatmap showing pairwise gene expression correlations across cell types in arteriole and thoracic aorta, with color indicating Spearman correlation coefficients. **E** Dot plot showing significant associations between cell types and blood pressure-related traits from MAGMA cell typing analysis. Statistical significance was assessed using a gene set enrichment analysis based on the top 10% most specific genes for each cell type. *P*-values were adjusted using the Benjamini-Hochberg (BH) method to control the false discovery rate (FDR). Only associations with FDR < 0.05 are shown. Dot size represents the effect size (beta), and color intensity reflects the magnitude of the $-\log_{10}(p\text{-value})$. Exact *p* values are in the Source Data file Cell type. EC endothelial cell, LEC lymphatic endothelial cell, VSMC vascular smooth muscle cell.

Roadmap Epigenomics projects. More than 90% of the chromatin loops in arterioles and EDAs, defined by global Micro-C, contained regulatory elements in both contact regions, 8.4% contained regulatory elements in one of the two contact regions, and only a small fraction did not contain any regulatory elements in their contact regions (Fig. 2C). The overlap of chromatin contact regions and regulatory elements was substantial as only 12% to 18% of the genome was covered by the contact regions and 16% covered by the regulatory elements. As we used regulatory elements from a broad range of cell types available in the Ensembl database, it is possible that the overlaps of arteriole chromatin contact regions with regulatory elements were overestimates, although the enrichment is likely true as the degree of enrichment is very high.

We grouped the chromatin loops in arterioles and EDAs into those involving enhancer-enhancer (EE), promoter-promoter (PP), enhancer-promoter (EP), enhancer-transcription factor binding site (ET), promoter-transcription factor binding site (PT), and transcription factor binding site- transcription factor binding site (TT) interactions (Fig. 2D). All types of chromatin contacts were associated with higher expression of nearby genes (Fig. 2E).

Based on the pan-promoter capture Micro-C analysis, the vast majority (89–96%) of chromatin regions interacting with gene promoters contained known regulatory elements (Supplementary Fig. S6A). 72% of the chromatin regions interacting with gene promoters contained enhancers, and 15% contained transcriptional factor binding sites (Supplementary Fig. S6B). RNA abundance was highly significantly correlated with the number of chromatin regions interacting with gene promoters ($p < 2 \times 10^{-16}$) (Fig. 2F). The average number of chromatin interactions was 3.8 per gene.

Representative genes with or without established roles in arteriolar function

We examined promoter chromatin interactions, DNA methylation, and RNA abundance for several genes essential for arteriolar function. *AGTR1* (Angiotensin II Receptor Type 1) had greater expression in intact arterioles and EDA than in arteriolar endothelial cells (Fig. 3A). We detected interactions of *AGTR1* promoter with intergenic genomic segments 100 kbp and 50 kbp upstream in intact arterioles and EDA, respectively (Fig. 3A). One of these interacting regions contained known enhancers based on Ensembl annotation. In EDA, *AGTR1* promoter also interacted with a genomic region nearly 600 kbp downstream of *AGTR1* (Fig. 3A). This genomic region contained known enhancers and binding sites for transcriptional factors and the CCCTC-binding factor (CTCF) important for chromatin conformation and transcriptional regulation.

In contrast, *EDN1* (Endothelin-1) and *NOS3* (Nitric Oxide Synthase 3) transcripts were abundant in intact arterioles and endothelial cells but much less so in EDA (Fig. 3B, C). For *EDN1* promoter, interactions with a genomic segment 300 kbp downstream of the gene were detected in both arterioles and EDA (Fig. 3B). Additional interacting regions 600 kbp upstream and 100 kbp downstream of the gene were detected in arterioles and EDA, respectively. All these interacting regions contained known enhancers, open chromatin regions, or binding sites for CTCF. The genomic region surrounding *EDN1* had more DNA methylation in EDA than in arterioles and endothelial cells (Fig. 3B). For *NOS3* promoter, interacting regions were detected 150 kbp downstream and 200 kbp upstream in arterioles and EDA, respectively, and these regions contained known enhancers, binding sites for transcriptional factors and CTCF, or open chromatin regions (Fig. 3C). The *NOS3* gene body had more DNA methylation in EDA than in arterioles and endothelial cells.

Next, we examined promoter chromatin interactions and DNA methylation for select genes without established roles in arteriolar function. Focusing on genes that were abundantly expressed in arteriolar tissues, we examined *SNRNP27* (Small Nuclear Ribonucleoprotein U4/U6.U5 Subunit 27) and *LGI4* (Leucine Rich Repeat LGI Family Member 4) (Supplementary Fig. S7). The promoter region of *SNRNP27* interacted with genomic segments 126 kbp and 186 kbp downstream and 112 kbp upstream of the promoter region in both arterioles and EDA. The promoter region of *LGI4* interacted with a genomic segment 53 kbp downstream in both arterioles and EDA but interacted with several other genomic segments that were unique to arterioles or EDA.

These findings reveal specific chromatin interactions and DNA methylation that may play a role in regulating the expression of several genes essential to arteriolar function or abundantly expressed but without established functional roles in arterioles.

Chromatin contact regions in human arterioles are enriched for BP-associated SNPs

To investigate the relation between arteriolar chromatin architecture and genetic determinants of arteriole-related phenotypes, we integrated the Micro-C and pan-promoter capture Micro-C data with an analysis of GWAS SNPs associated with arteriole-related traits, including systolic BP, diastolic BP, pulse pressure, essential hypertension, stroke, peripheral arterial disease, diabetic nephropathy, and diabetic retinopathy. By examining the overlap between these SNPs and chromatin interaction regions in both intact arterioles and EDA, we observed that SNPs associated with systolic BP, diastolic BP and pulse pressure were consistently enriched in chromatin contact regions compared to SNPs linked to non-arteriole-related traits (all *p*-values < 0.01) (Fig. 4A; Methods). Additionally, stroke-associated SNPs were significantly enriched in chromatin contacts in intact arteriole ($p = 0.045$), but not in EDA, consistent with a prominent role of endothelial cells in stroke pathogenesis. Our arteriole-based Micro-C data showed a higher capture of BP-associated SNPs per 1Mbp loop contact region compared to Hi-C data from tibial arteries and aorta in ENCODE[7] (Fig. 4B), which might be due to differences between tissues, assay protocols, or both.

Further analysis of SNPs associated with arteriole-related traits and their interacting genes, captured through our chromatin contacts, identified a total of 10,217 SNP-gene pairs (Supplementary Data S15). Notably, 8,011 of these pairs had not been previously reported in the GWAS Catalog or revealed through eQTL analysis by GTEx in large arteries, including aorta, tibial artery, and coronary artery, highlighting the additional information provided by chromatin interaction analysis. Nevertheless, the overlap between SNP-gene pairs identified by arteriolar chromatin interactions and large artery eQTL data was 938, a

https://doi.org/10.1038/s41467-025-61656-7

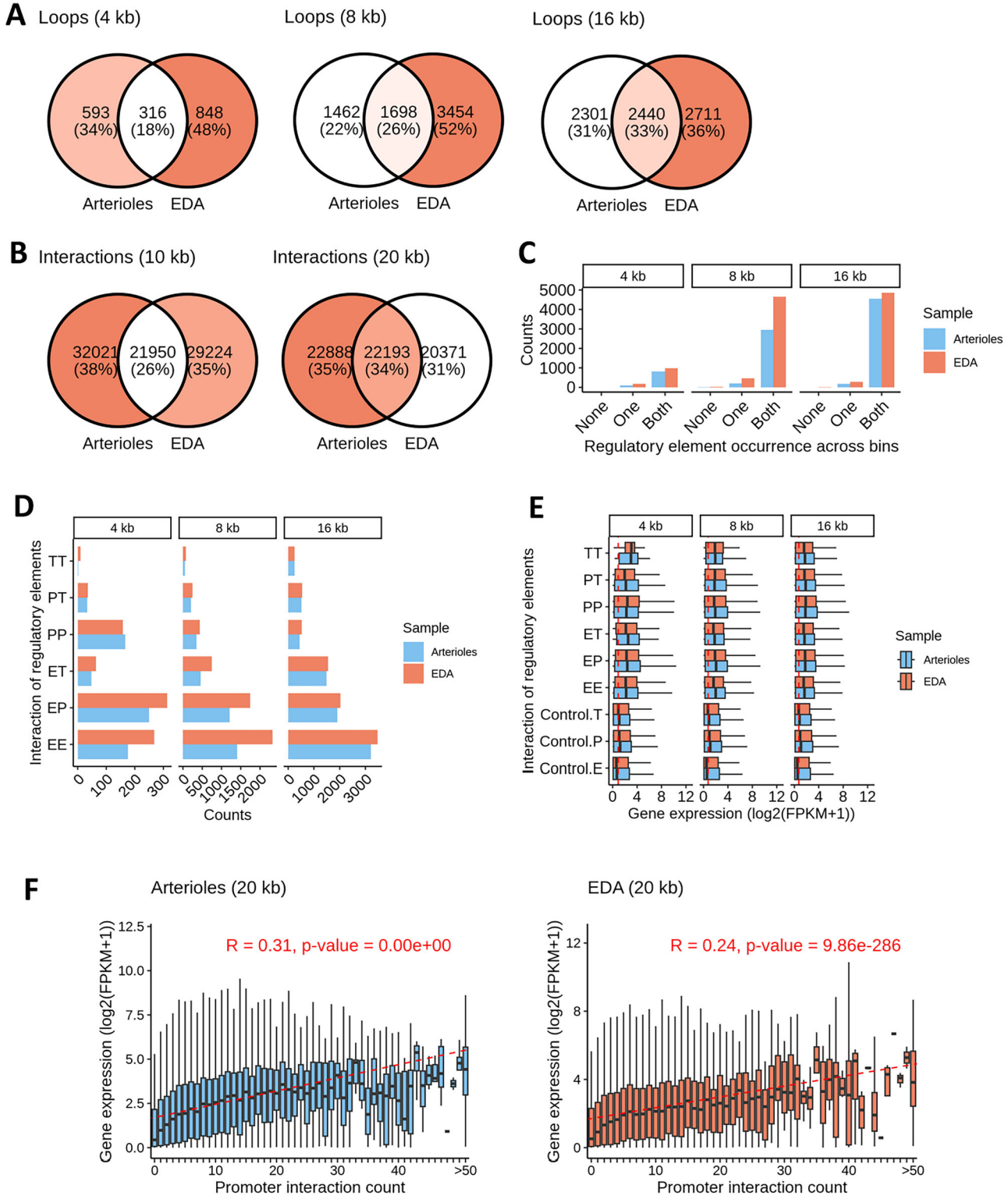

significant overlap compared to all arteriolar trait-associated SNPs linked to genes within 2 Mbp ($p < 2 \times 10^{-16}$), supporting a regulatory role of chromatin interactions in eQTLs (Fig. 4C). Among these overlaps, 522 were not listed as nearby genes in the GWAS Catalog. Additionally, an average of 344 long-distance SNP-gene interactions (>100 kb) were identified in the Micro-C data, while an average of 3,331 long-distance interactions were identified in the pan-promoter capture Micro-C data (Fig. 4D). Functional enrichment analysis of genes interacting with SNPs via chromatin contacts, based on the pan-promoter capture Micro-C data, showed significant enrichment in muscle system processes and tissue development in arterioles. In the EDA dataset, enriched pathways were related to cellular response to external stimuli, including hormone and peptide responses, apoptotic signaling and hypoxia (Fig. 4E).

Enhancer SNP-promoter interactions linked to cell type specific gene expression

In our pan-promoter capture Micro-C data, each interaction includes a captured promoter bin and a distal interacting bin (Supplementary Datas S11–S14). An average of 86% of the SNPs in the captured SNP-

Fig. 2 | Chromatin contact regions in human arterioles contain DNA regulatory elements and correlate with greater gene expression. A Venn diagrams showing the overlap between loops identified in arterioles and EC-denuded arterioles (EDA) by Micro-C at 4 kb, 8 kb, and 16 kb resolutions. **B** Venn diagrams showing the overlap between interactions identified in arterioles and EDA by pan-promoter Capture Micro-C at 10 kb and 20 kb resolutions. **C** Bar plot showing the number of loops with regulatory elements present in one or both chromatin contact regions in arterioles and EDA across resolutions. "None," "one," and "both" indicate the presence of regulatory elements in neither, one, or both interacting regions, respectively. **D** Number of chromatin interactions classified by interaction type: promoter-promoter (PP), enhancer-promoter (EP), enhancer-enhancer (EE), enhancer-transcription factor binding site (ET), promoter-transcription factor binding site (PT), and transcription factor binding site-transcription factor binding site (TT). Categories are not mutually exclusive. **E** Expression levels of genes proximal to chromatin interactions (within 5 kb upstream or downstream of contact regions), grouped by interaction type (PP, EP, EE, ET, PT, TT). Controls include genes proximal to regulatory regions, including promoters, enhancers, or transcription factor binding sites, that were not in contact regions based on our data. Each box summarizes gene-level data. The number of genes (n) per category varies and is provided in the Source Data file. Boxes represent the interquartile range (IQR, 25th to 75th percentile), center line shows the median, and whiskers extend to 1.5 × IQR. **F** Boxplot showing gene expression levels grouped by the number of chromatin interactions involving gene promoter regions. Spearman correlation was applied. Each box summarizes gene-level data. The number of genes (n) per category is provided in the Source Data file. Boxes represent the IQR (25th to 75th percentile), center line shows the median, and whiskers extend to 1.5 × IQR.

gene pairs were in the distal interacting bin (6192 out of 7216 and 5567 out of 6427) (Fig. 4F). These SNPs were significantly enriched in enhancer regions (all p-values < 0.001), suggesting that SNPs frequently exert their influence on gene promoter via enhancer regions when mediated by chromatin interactions (Fig. 4G).

To assess potential impact of SNPs on gene expression through promoter interaction in a cell type specific manner, we investigated two scenarios: 1) arteriole-specific SNP-gene interactions involving EC enriched genes (Fig. 4H), and 2) SNP-gene pairs shared between arteriole and EDA that involve genes enriched in non-EC cell types (Fig. 4I). Among the 1367 EC-enriched genes identified from arteriole snRNA-seq data (Bonferroni-adjusted p-value < 0.05 and |log2 fold change| > 0.25), 102 genes were involved in SNP-gene interactions, with 26 of them having promoter interactions with enhancer-located SNPs. Notable examples include rs2836411-*ERG* and rs2244643-*FBLN5* (Fig. 4H). *ERG* regulates angiogenesis and vascular stability by promoting VE-cadherin expression and Wnt/β-catenin signaling, ensuring endothelial integrity and survival[16,17]. *FBLN5* has been reported to be involved in the adaptive response of endothelial cells to hypoxia[18]. Both *ERG* and *FBLN5* showed strong endothelial expression (Fig. 4J), and *ERG* was significantly more highly expressed in arterioles compared to DEA in bulk RNA-seq (FDR = 0.002). Among non-EC cell types, fibroblasts had the largest number of SNP-interacting genes enriched in this cell type, including top enhancer SNP-gene interactions such as rs2251636-*SEMA4A* and rs11725926-*PDGFRA* (Fig. 4I). *SEMA4A* has been reported to promote fibrosis across multiple disease contexts[19,20], while *PDGFRA* is involved in fibroblast-to-myofibroblast transition[21]. Together, these findings underscore the potential of chromatin interactions to mediate the cell type-specific regulatory effects of genomic variants on gene expression.

BP-associated SNP rs1882961 interacts with *NRIP1* promoter in human arterioles and regulates NRIP1 expression

The above findings suggested that SNPs might influence arteriole-related phenotypes by regulating genes whose promoters interacted with the SNPs across long genomic distances. In a proof of principle study, we experimentally investigated a selected BP-associated SNP. There were 8790 pairs of arteriolar trait-associated SNPs and genes whose promoters interacted with the genomic regions containing these SNPs based on our arteriolar and EDA pan-promoter capture Micro-C dataset. We filtered these pairs based on both biological and technical criteria (Fig. 5A). The biological criteria included BP-associated SNPs, promoters of protein-coding genes, low promoter methylation levels (beta value < 0.2), and RNA abundance above a minimum threshold (average $\log_2(\text{FPKM}+1) > 1$). Technical criteria included not being in linkage disequilibrium with other SNPs for ease of genomic editing, cross-species conservation of the SNP genomic region to facilitate studies in animal models, and genes paired with only one SNP to avoid confounding effects from multiple variants. Furthermore, we focused on SNP-gene pairs for which the SNP is more than 100 kbp away from the gene as it is particularly challenging to identify the effector genes for these SNPs and understand the genomic mechanisms involved. These filters narrowed the list of SNP-gene pairs down to 89, from which we performed experimental studies on rs1882961 and *NRIP1* based on additional considerations of GWAS significance, mapping specificity (single SNP-gene association), gene expression levels in snRNA-seq data, and known functions of the genes involved.

rs1882961 is associated with systolic BP[22]. The genomic region containing rs1882961 interacted with *NRIP1* promoter region in EDA (Fig. 5B). The transcription start site of *NRIP1* is 119 kbp from rs1882961 (Fig. 5C). *NRIP1* encodes nuclear receptor interacting protein 1, also known as receptor-interacting protein 140 (RIP14). RIP140 is a co-regulatory for most nuclear receptors including retinoic acid receptor, estrogen receptor, and thyroid hormone receptor, many of which could influence vascular function[23]. However, the involvement of *NRIP1* in blood pressure regulation and the role of rs1882961 in the regulation of *NRIP1* are unknown.

We experimentally examined the allelic effect of rs1882961 on the expression of *NRIP1* and other local genes *SAMSN1* and *USP25* in human vascular smooth muscle cells (Fig. 5C). To that end, we generated isogenic hiPSCs precisely edited to contain homozygous rs1882961-C (low-BP allele) or rs1882961-T (high-BP allele) (Fig. 5D, E; Supplementary Figs. S8, S9). The edited hiPSCs were differentiated to vascular smooth muscle cells (iVSMCs) (Supplementary Fig. S10A, B). The successful generation of iVSMCs was confirmed through the expression of VSMC marker genes, including Actin Alpha 2, Smooth Muscle (*ACTA2*), Calponin 1 (*CNN1*), and Smoothelin (*SMTN*) (Supplementary Fig. S10C). In iVSMCs, *NRIP1* and *SAMSN1* were significantly upregulated in cells with the high-BP allele of rs1882961 compared with the low-BP allele (Fig. 5F). *USP25* was not differentially expressed. We performed region-capture Micro-C analysis to capture any genomic segment interacting with rs1882961 or promoters of its neighboring genes. The analysis revealed greater chromatin interactions between the rs1882961 genomic region and the promoter regions of *NRIP1* and *SAMSN1*, but not *USP25*, in iVSMCs with the high-BP allele than the low-BP allele (Fig. 5G).

A 4-bp segment encompassing the rs1882961 orthologous site alters BP in SS rats

We tested the effect of the rs1882961 genomic site on BP and *Nrip1* expression in vivo. We mapped rs1882961 to position chr11:15,091,368 in the rat genome, which is 112 kbp from the TSS of *Nrip1* (Fig. 6A; Supplementary Fig. S11). A 500-bp region around the SNP site is conserved across vertebrates. For the 60 bp around the SNP site, only 5 mismatches are present between the human and rat reference genomes (Supplementary Fig. S11). We successfully deleted a 4-bp segment that encompassed the rs1882961 orthologous site from the genome of the Dahl salt-sensitive (SS) rat using CRISPR/Cas9 (Fig. 6A; Supplementary Fig. S11). The mutant strain was designated SS-Δrs1882961. We phenotyped female rats as the hiPSCs used in the study above were derived from a female subject. Mean

https://doi.org/10.1038/s41467-025-61656-7

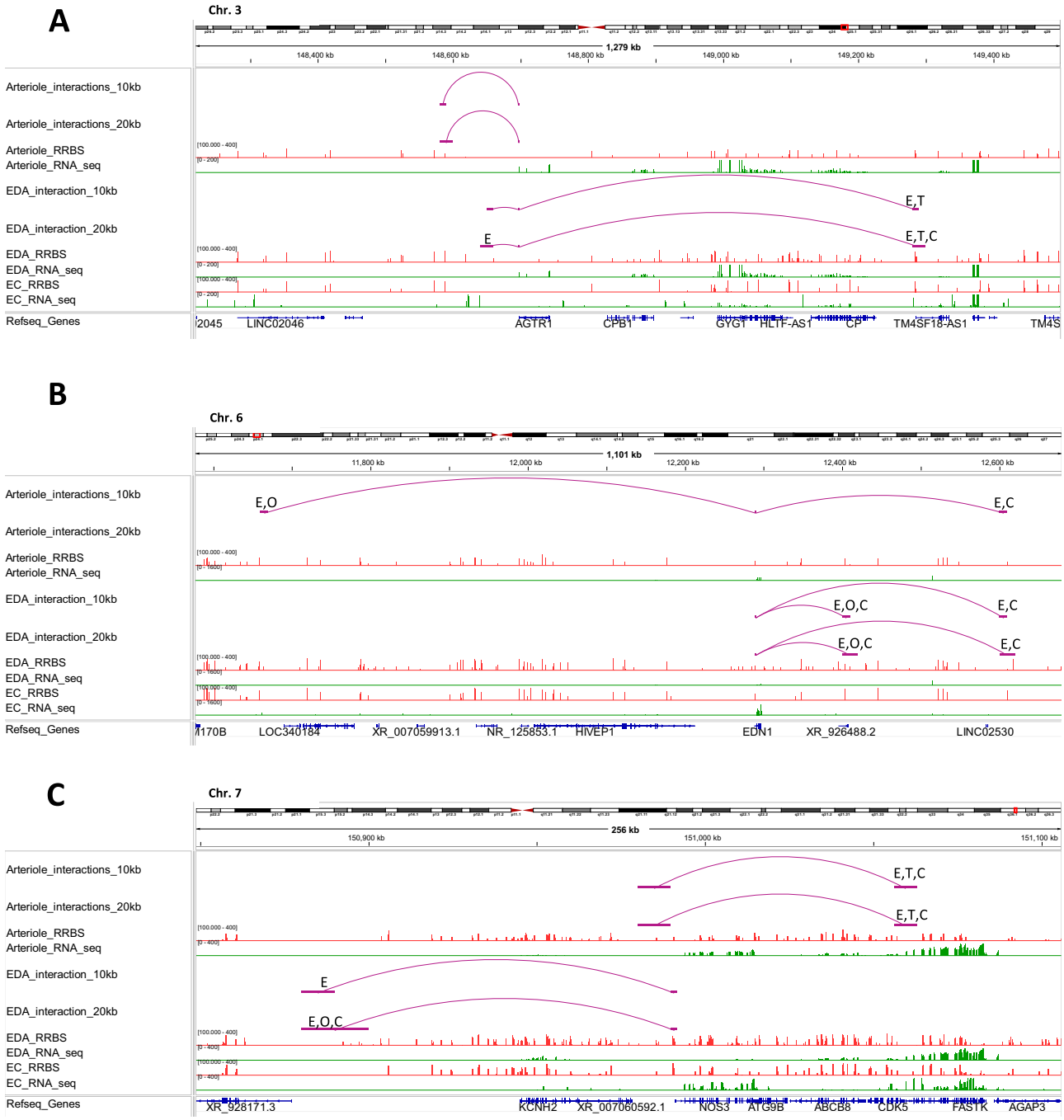

Fig. 3 | Chromatin interactions with gene promoters, DNA methylation, and mRNA abundance of representative genes essential to arteriolar function. **A** *AGTR1* (Angiotensin II Receptor Type 1). **B** *EDN1* (Endothelin 1). **C** *NOS3* (Nitric Oxide Synthase 3). Linux-based IGV was used to plot chromatin interactions based on pan-promoter capture Micro-C, RNA abundance based on poly(A)-dependent RNA-seq, and methylation levels based on RRBS. Only chromatin interactions with the promoter of the gene of interest are shown. The chromatin contact regions were compared with the regulatory elements as defined by Ensembl for overlaps. E enhancer, T transcriptional factor binding site, C CCCTC-binding factor (CTCF) binding site, O open chromatin region.

arterial pressure, systolic BP, diastolic BP, and pulse pressure, but not heart rate, in SS-Δrs1882961$^{-/-}$ rats was significantly lower than wild-type littermate SS rats after the rats had been fed a high-salt (4% NaCl) diet (Fig. 6B–F). The difference of mean arterial pressure occurred primarily in the dark phase (i.e., active phase) in a light-dark cycle, reaching approximately 15 mmHg during part of the dark phase (Fig. 6G).

Nrip1 expression in mesenteric tissue was up-regulated in response to the high-salt diet but to a lesser extent in SS-Δrs1882961$^{-/-}$ rats, resulting in significantly lower expression in SS-Δrs1882961$^{-/-}$ rats than in wild-type SS rats on the high-salt diet (Fig. 6H). However, there was no change in *Nrip1* expression in the aortic tissue of SS-Δrs1882961-/- rats compared to WT (Supplementary Fig. S12). Vasodilation of the third-order mesenteric arteries in response to spermine NONOate, an nitric oxide (NO) donor, was significantly improved in SS-Δrs1882961$^{-/-}$ rats compared with SS littermates (Fig. 6I), suggesting that vascular smooth muscle sensitivity to NO is improved by rs1882961 orthologous segment deletion.

These studies demonstrate that a 4-bp segment of noncoding DNA encompassing the rs1882961 orthologous site regulates the

https://doi.org/10.1038/s41467-025-61656-7

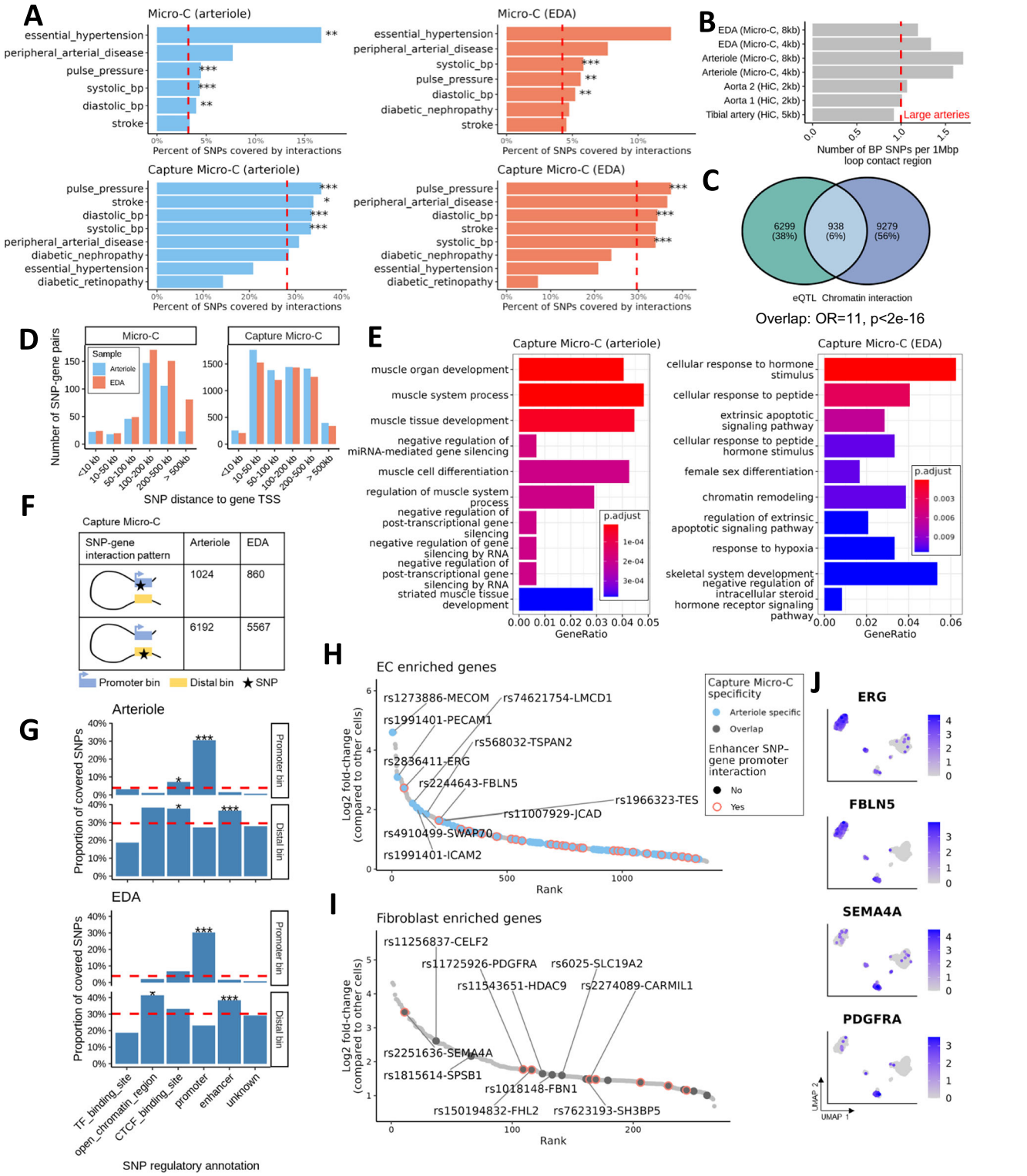

expression of *Nrip1* 112 kbp away in vivo and influences vascular function and the development of salt-induced hypertension.

Discussion

Long-range chromatin interactions play an important role in the regulation of gene expression[24,25]. We have found that, in human arterioles, regulatory elements are prevalent in chromatin contact regions and the frequency of long-range chromatin interaction with gene promoters is highly significantly correlated with RNA abundance. These findings indicate that long-range chromatin interaction may be a here-to-fore unrecognized mechanism underlying the essential physiological function and broad pathophysiological relevance of arterioles. In addition, we found pericytes to be a prominent cell type in arterioles, and genes enriched in arteriolar pericytes significantly overlapped with genes linked to diastolic BP-associated genomic variants. These findings suggest that the functional significance of arteriolar pericytes warrants greater attention in future studies. We envision that our extensive dataset will drive forward mechanistic studies of hypertension, stroke, microvascular complications of diabetes and hypertension, and other arteriole-related diseases in new directions.

Fig. 4 | Chromatin contact regions in human arterioles are enriched for SNPs associated with blood pressure and stroke. A Bar plot showing the percentage of SNPs covered by Micro-C or pan-promoter Capture Micro-C in arterioles and EDA, grouped by arteriole-related traits. Red dashed lines indicate the average SNP coverage across non-arteriole-related traits (Methods). One-sided binomial test; no multiple testing correction. **B** Bar plot of BP-associated SNPs density within 1 Mb contact regions in our Micro-C datasets compared to Hi-C from the tibial artery and aorta (ENCODE). Red dashed line represents average SNP density in Hi-C. **C** Venn diagrams showing overlap of SNP-gene pairs identified by chromatin interactions and GTEx artery eQTLs (aorta, tibial, coronary). Two-sided Fisher's exact test against all arteriolar trait-associated SNPs linked to genes within ±2 Mbp; unadjusted *p*-values. **D** Bar plot of SNP-gene interaction distances, binned by distance categories. Only SNPs from arteriole-related traits (see **A**) are included. **E** Pathway enrichment of genes interacting with arteriole-related SNPs in pan-promoter Capture Micro-C, shown for arteriole and EDA. BH method applied for FDR correction. **F** Schematic of SNP-gene interaction patterns by SNP bin location (promoter vs. distal), with interaction counts in arterioles and EDA. **G** Percentage of covered SNPs by regulatory elements (promoter vs. distal). Red dashed lines represent overall SNP coverage. Two-sided Fisher's exact test with BH correction; only significant enrichments with odds ratio > 1 are marked with asterisks. Rank plot of genes significantly upregulated in ECs (**H**) and fibroblasts (**I**) compared to all other cell types (one-sided Wilcoxon test; Bonferroni-corrected *p*-value < 0.05). Genes involved in SNP-promoter interactions are colored by occurrence. Enhancer SNP-promoter targets are highlighted with red circles. Top 10 SNP-gene pairs are labeled. **J** UMAP plots showing the expression of selected enhancer SNP-linked genes (*ERG*, *FBLN5*, *SEMA4A* and *PDGFRA*) across arterioles cell types (snRNA-seq data). Statistical significance is indicated as follows: $*p < 0.05$, $**p < 0.01$, and $**p < 0.001$. Exact *p* values are in the Source Data file.

Long-range chromatin interactions are especially relevant to understanding the mechanisms by which noncoding sequence variants identified by GWAS influence their associated traits as many GWAS variants are located 10 s of kbp from their nearest genes[26,27]. The approach that we used in this study integrates in-depth chromatin conformation analysis in trait-relevant human tissues with analysis of GWAS-nominated SNPs, in vivo and in vitro genome editing, and functional investigation. The analysis revealed significant enrichment of SNPs associated with systolic BP, diastolic BP, pulse pressure, and stroke in chromatin contact regions in arteriolar tissues, supporting the relevance of arteriolar chromatin interactions in the genetic regulation of these specific traits. Further integration with snRNA-seq data highlighted the potential of arteriolar chromatin interactions to mediate the cell type-specific regulatory effects of vascular trait-associated genomic variants on gene expression. As demonstrated by our proof of principle study of rs1882961, this integrated approach is powerful and can be applied broadly to bridge the critical gap between genetic discoveries and physiological understanding.

It is remarkable that deletion of a mere 4 bp at a genomic site that is more than 100 kbp from the transcription start site of the nearest protein-coding gene changes hourly BP by up to 15 mmHg. The high-salt dietary challenge and possibly the genomic background of the SS rat may have contributed to the uncovering of this remarkable BP effect. By extrapolation, the SNP rs1882961 and other GWAS-nominated sequence variants may have greater effects on BP and other associated traits in groups of humans with permissive genomic backgrounds and exposed to certain stressors than the typically minute effect reported by GWAS. In addition, such robust phenotypic changes, along with the changes in *Nrip1* expression in the mutant rat and edited cells, not only reenforce the significance of long-range chromatin interaction in genetic and molecular regulation but also support its relevance to the regulation of physiological function. It is important to recognize that the robust BP effects were observed in the context of salt-induced hypertension in this study, and it remains to be investigated whether these effects are relevant to other types of hypertension.

This study is one of the first to apply Micro-C and capture Micro-C techniques to analyze human tissues[28,29]. The data was robust, considering the limited input material compared with studies using cultured cells. We performed our chromatin interaction analyses, as well as DNA methylation analysis, in bulk tissues. While techniques for analyzing chromatin conformation and DNA methylation in single nuclei have been reported[30–32], they require much more input materials than available from human arterioles, and data from these assays is sparser than from bulk tissue assays. Moreover, single-nucleus methods are not available for promoter capture Micro-C. Meanwhile, the robustness of our bulk tissue data is enhanced by the relative simplicity of cell type composition in arteriole compared to more complex organs. Additionally, we reduced the tissue complexity by analyzing separate tissue components in the current study.

We analyzed arterioles isolated from subcutaneous fat. Pathological changes in subcutaneous vessel structure and physiology are well-established to reflect the influence of cardiovascular risk factors and prevalent cardiovascular disease[33–37]. Physiological similarities and differences exist between arterioles in subcutaneous fat and those in visceral fat or internal organs[34,38,39]. It would be valuable to analyze arterioles in other tissue depots in future studies. Nevertheless, the reference molecular profiles generated in the current study will help to drive studies of arteriole-related traits and diseases in general as our study of rs1882961 has demonstrated. In addition, we chose to use subcutaneous fat because of the relative ease of obtaining such specimens from human participants, including via a minimally invasive biopsy in healthy individuals[40]. This means our data will be directly relevant to large-scale studies of human arterioles in which the ease of tissue procurement is particularly important.

Methods

The human research protocols were approved by the Medical College of Wisconsin Institutional Review Board (IRB). The animal protocols were approved by the Institutional Animal Care and Use Committee at the Medical College of Wisconsin (AUA00000206, AUA00002214).

Human arterioles

Human arterioles were obtained from discarded subcutaneous adipose tissue from surgery as described with modifications[40]. All protocols were approved by the Medical College of Wisconsin Institutional Review Board (IRB). Subject inclusion criteria were age 18-89 and without major cardiovascular diseases except for hypertension. Exclusion criteria were coronary heart disease, heart failure, COVID19 infection within one-year, current tobacco use, and cancer chemotherapy drug exposure. The subjects involved in this study included a mix of age, race, sex, and hypertension status for the goal of generating reference omic profiles for subjects meeting the inclusion/exclusion criteria. Detailed information about the subjects is available in Supplementary Data S1. Immediately upon receiving the discarded tissue, arterioles were isolated in cold (4 °C) HEPES buffer by removing the surrounding fat and connective tissue. These intact isolated arterioles were snap-frozen in liquid nitrogen and stored at −80 °C until use. For arterioles undergoing endothelial cell scraping, the isolated arterioles were cut open along their longitudinal direction with fine scissors and fixed lumen side-up with fine pins on a peri dish coated with silicone gel. After washing two times with PBS, the endothelial layer at the top of the lumen side was scrapped with a blade. After scraping, the blade was rinsed in an Eppendorf tube containing 700 μl of PBS; 800 μl of PBS was used to rinse the scrapped lumen side and collected into the same Eppendorf tube. The tube was spun at 300 g at 4 °C for 10 min. The pellet with 100 μl of supernatant was snap-frozen in liquid nitrogen and stored at −80 °C until use. The vascular tissue that remained after the scraping was also collected as endothelium-denuded arteriole (EDA).

https://doi.org/10.1038/s41467-025-61656-7

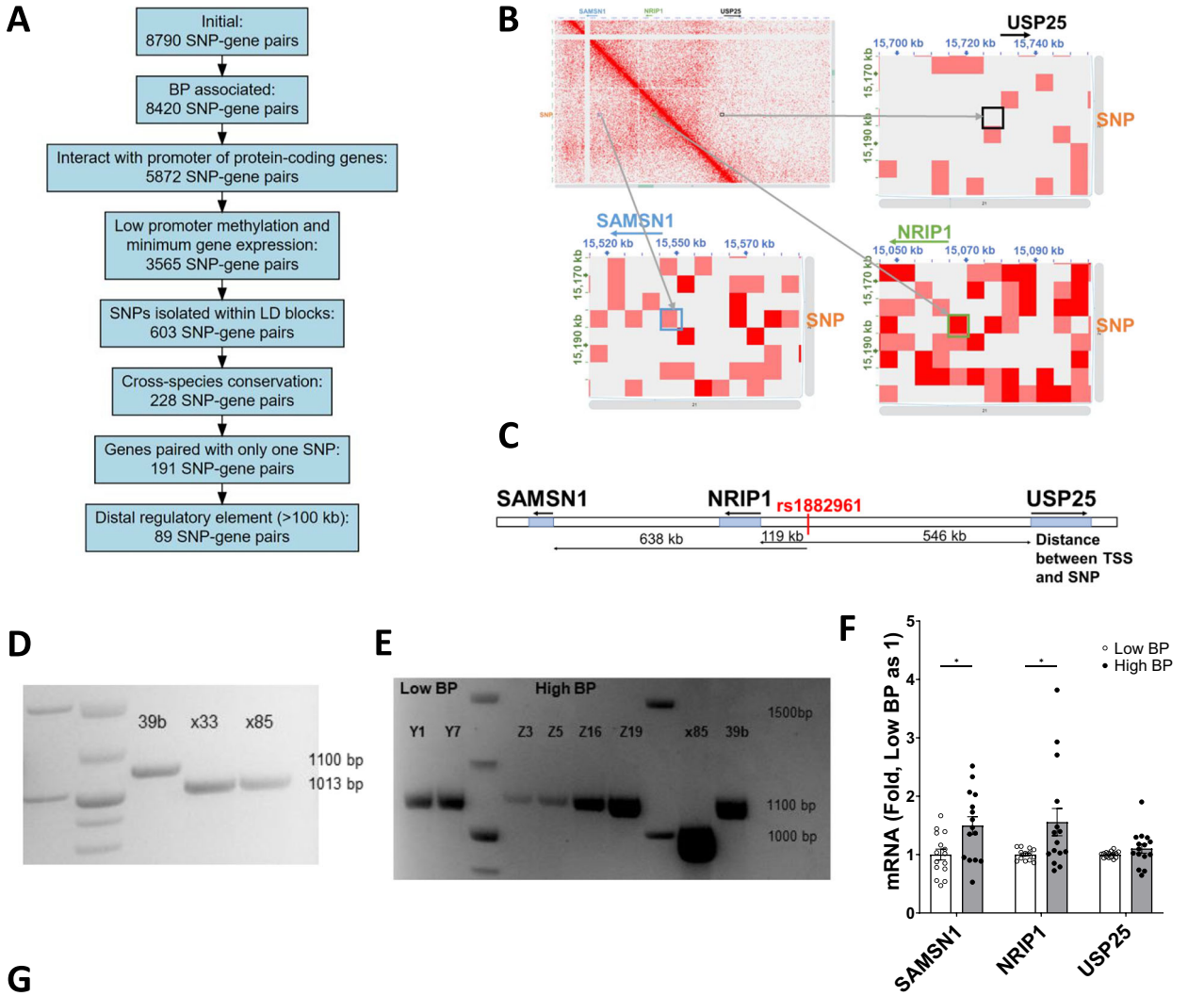

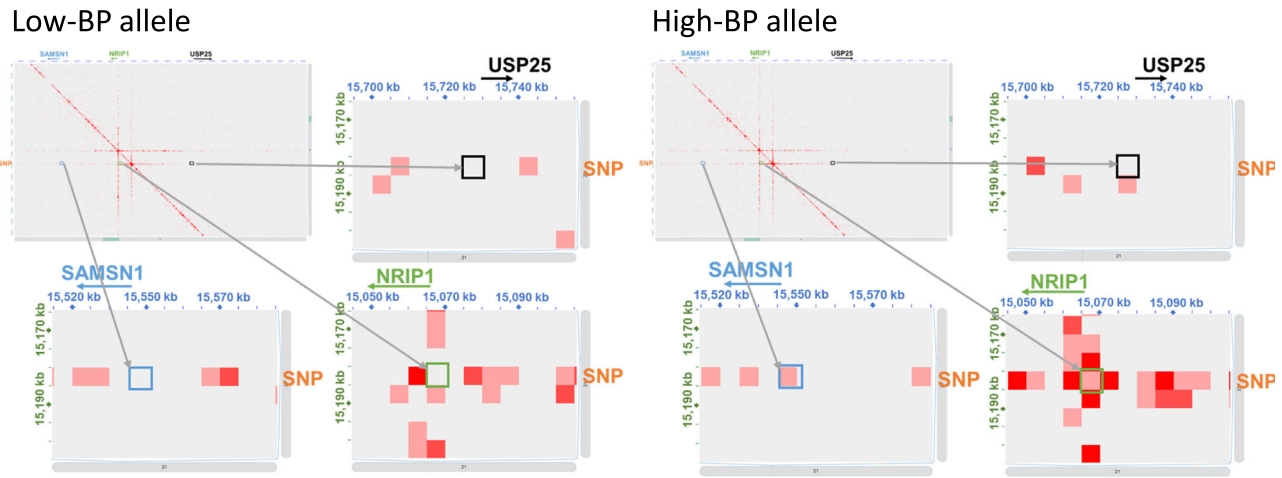

Micro-C assay and data analysis

Micro-C assay[29] was performed using Dovetail® Micro-C Kit following manufacturer's User Guide for Tissue and Blood to create Micro-C libraries. Briefly, tissues were ground into fine powder with CryoGrinder™. The ground tissue was crosslinked with disuccinimidyl glutarate and formaldehyde sequentially. The genomic DNA was digested in situ with MNase Enzyme mix to 20%–40% mononucleosomes. Genomic DNA was released from cells and put through a sequential process of binding to chromatin capture beads, end polishing, bridge ligation, intra-aggregate ligation, crosslink reversal, and DNA purification. Library was made from the purified DNA and subject to sequencing with Novaseq 6000 platform for approximately 800 M 150 PE reads.

Pair-end sequencing reads were cleaned with Trim Galore (v0.6.2) to remove adaptor and low-quality reads. We used JuicerBox, which was a one-click pipeline for processing HiC or Micro-C data, to generate hic file for direct visualization[41]. We followed Dovetail Micro-C Data Processing Guide to generate.mcool file and used it for loop calling with Mustache[42].

Fig. 5 | BP-associated noncoding SNP rs1882961 interacts with NRIP1 promoter 119 kbp away and influences NRIP1 expression. A Prioritization of SNP-gene pairs for experimental analysis. **B** The genomic region containing rs1882961 interacted with *NRIP1* promoter 119 kbp away from it in human endothelium-denuded arterioles, based on pan-promoter capture Micro-C analysis. **C** Local gene organization around rs1882961 in the human genome. **D** Deletion of DNA segment containing rs1882961. 39b, original iPSC cell line; X33 and X85, rs1882961-deleted cell lines. **E** Reconstitution of the rs1882961 locus containing either homozygous low BP allele or high BP allele. 39b, original iPSC cell line; X85, rs1882961-deleted cell line; Y series, cell lines with reconstituted low-BP rs1882961 allele; Z series, cell lines with reconstituted high-BP rs1882961 allele. See Supplementary Fig. S8 for sequence confirmation. **F** Homozygous high-BP allele of rs1882961, reconstituted in hiPSCs, increased *NRIP1* and *SAMSN1* expression in isogenic hiPSC-derived vascular smooth muscle cells (iVSMCs). Each line of hiPSCs was differentiated to iVSMCs in five independent rounds with three independent wells in each round, with each well considered a replicate. For *SAMSN1* and *NRIP1* expression, $N = 13$ for low BP and $N = 15$ for high BP; for *USP25*, $N = 15$ for low BP and $N = 15$ for high BP; Data are presented as Mean ± SEM. *, $p = 0.0095$ for *SAMSN1* and $p = 0.0371$ for *NRIP1* -, two-tailed unpaired t-test. **G** Region-capture Micro-C analysis showed greater chromatin interactions between the rs1882961 region and the promoters of *SAMSN1* and *NRIP1* in iVSMCs with the high-BP allele of rs1882961, compared to iVSMCs with the low-BP allele. Each square color box in the zoom-in images is 5 kbp x 5 kbp.

Pan-promoter capture Micro-C assay and data analysis

Pan-promoter capture Micro-C library was created using the Micro-C libraries generated as described above, Dovetail® human Pan Promoter Enrichment panel, and Dovetail Target Enrichment kit. The panel included 161,144 probes designed to cover 84,643 promoters for 19725 protein-coding genes and 7630 long noncoding genes in human based on Ensembl GRCh38 version 86. The libraries were sequenced using the Illumina NovaSeq sequencers.

The data were analyzed following Dovetail Promoter Panel Data Processing Guide to generate mapped.PT.bam file. Direct chromatin interactions were then identified by CHiCAGO at different resolutions with the mapped.PT.bam file[43]. To ensure our dataset aligned with the most current promoter definitions, we updated the transcript promoter annotations using the latest Ensembl GRCh38 version 112. Following this update, we retained 99% of the original chromatin interactions that captured promoter regions (Supplementary Data S10). These retained interactions were used in the subsequent analysis. Genomic overlap analysis was performed using the GenomicRanges R package (v1.50.2). Regulatory element annotations were downloaded from Ensembl. To maintain consistency with the promoter definition used in Dovetail, promoter regions in the pan-promoter Capture Micro-C data were defined as 1000 bp upstream and 500 bp downstream of transcript TSSs.

Hi-C data source and access

Pre-processed Hi-C loop data for the aorta and tibial artery were obtained from the ENCODE consortium. The data were accessed in the form of bedpe files from the following ENCODE experiment accessions: ENCSR797MWY, ENCSR554SLA (aorta), and ENCSR601RFS (tibial artery).

Poly(A)-dependent RNA-seq and data analysis

Poly(A)-dependent RNA-seq experiment and data analysis were performed as described[40]. An in-house pipeline was used to analyze RNA-seq data. Briefly, raw RNA-Seq sequence reads were pre-processed using Trim Galore (v0.6.2) (http://www.bioinformatics.babraham.ac.uk/projects/trim_galore/). Adapters and reads with low quality (base quality < 20) were removed prior to further analysis. The trimmed sequence reads longer than 20 bp were mapped to the human genome (hg38) using hisat2 (v2.2.1)[44]. Transcript assembly and quantification were performed using StringTie2 (v2.2.1)[45], based on the GENCODE reference annotation (v38). R package DESeq2 was used to identify differentially expressed genes (DEGs; FDR < 0.05), accounting for inter-subject variability (modeled as ~ Subject + Tissue)[46].

Reduced representation bisulfite sequencing (RRBS) and data analysis

DNA methylation profiles at single-base resolution were analyzing using multiplexed RRBS as we described[12,13,47]. Trimmed sequences were mapped to the human reference genome (hg38) using Bismark (v0.16.1)[48]. To account for inter-subject variability, modified metilene (Version 0.23) with paired Wilcoxon signed-rank test was applied to identify differentially methylated regions (DMRs) de novo[49]. Methylation rate of each region was calculated as the average methylation rate of each site across the region. Differentially methylated regions (DMR) were identified based on the following criteria: a minimum mean methylation difference between groups of 0.05, a minimum of three CpGs within the identified regions, and an FDR < 0.05 from the Wilcoxon signed-rank test.

Single-nucleus RNA-seq and data analysis

Human arterioles were broken up using a beads method, and nuclei were extracted using the 'Frankenstein' protocol. Briefly, the arterioles were broken up in 0.5 ml Nuclei EZ Lysis buffer with Precellys Evolution Touch and tissue homogenizing ceramic beads at a setting of 6500 rpm for 20 sec. Another 3.5 ml Nuclei EZ Lysis buffer was added to tissue homogenized buffer and incubated for 5 min on ice before being filtered through a 70 μm strainer mesh. The extracted nuclei were washed once with Nuclei Wash and Suspension Buffer. Single-nucleus RNA-seq libraries were prepared using Chromium Single Cell 3' Reagent Kits V3 (10x Genomics, Pleasanton, CA), following the manufacturer's user guide. snRNA-seq libraries were sequenced using the Illumina NovaSeq sequencers to generate approximately 30 GB or 100 million paired reads of data per library.

Raw fastq files were processed using CellRanger (v7.0.0) to generate feature matrices using 10x Genomics reference genome assembly hg38 (refdata-gex-GRCh38-2020-A). DoubletFinder R package (v2.0.3) was used to remove potential doublets, with the doublet rate set to max(0.3, #cells*8*1e-6)[50]. Cells with less than 200 genes or a mitochondrial percentage larger than 20% were excluded from the analysis.

For quality-controlled snRNA-seq data, the gene count matrix was log-transformed and scaled. The top 2000 most variable genes were identified using the FindVariableFeatures function from Seurat R package (v4.3.0.1)[51], and then were used for principal component analysis (PCA). Clustering was performed using the top 20 principal components and the Louvain algorithm, with resolution adjusted from 0.5 to 2 in increments of 0.5. The optimal resolution was selected based on Clustree (v0.5.1) analysis[52]. To annotate identified clusters, differentially expressed genes (DEGs) between clusters were identified by Wilcoxon rank sum test using FindAllMarkers function (logfc.threshold = 0.25, min.pct = 0.25, only.pos = TRUE). Statistical significance was determined as a Bonferroni-adjusted p-value < 0.05 and an absolute log2 fold change >0.25. Canonical markers from PanglaoDB and CellMarker were referenced to annotate major cell types[53,54].

Preprocessed snRNA-seq data for the thoracic aorta was downloaded from https://singlecell.broadinstitute.org/single_cell/study/SCP1265, and cell clusters and annotations from the original study were applied[11].

To compare cell type expression similarity between arterioles and the thoracic aorta, pseudo-bulk RNA-seq profiles were generated for each cell type within each dataset using AverageExpression function. DEGs across cell types were calculated using the FindAllMarkers function, with significance determined by a Bonferroni-adjusted p-value < 0.05. Common DEGs across datasets were then used for pairwise Spearman correlation analysis to compare cell types between the two datasets based on their pseudo-bulk expression profiles.

https://doi.org/10.1038/s41467-025-61656-7

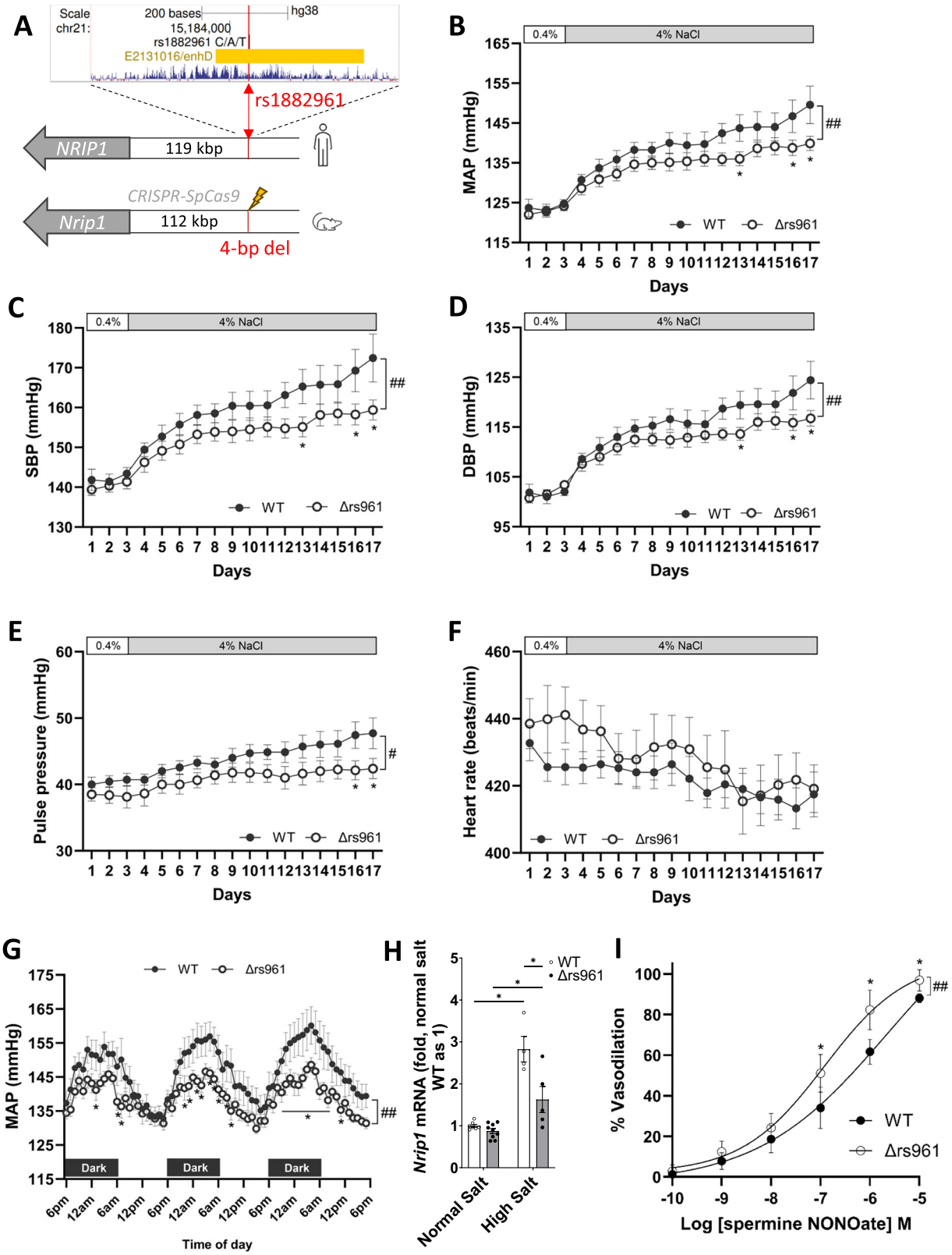

MAGMA cell typing

Preprocessed study-level GWAS summary statistics for blood pressure regulation and hypertension end-organ damage traits were downloaded from the GWAS Catalog (https://www.ebi.ac.uk/gwas/). This included systolic and diastolic blood pressure from studies by Keaton JM et al.[55], Surendran P et al.[56], and Wojcik GL et al.[57]; pulse pressure from Keaton JM et al.[55] and Surendran P et al.[56]; essential hypertension from Wojcik GL et al.[57]; stroke from Malik R et al.[58] and Mishra A et al.[59]; peripheral arterial disease from Sakaue S et al.[60]; diabetic nephropathy from Sakaue S et al.[60] and Zhou W et al.[61]; and diabetic retinopathy from Backman JD et al.[62] and Zhou W et al.[61]. Cell type-trait association analysis was performed using the celltype_associations_pipeline from the MAGMA.Celltyping R package (v2.0.11)[63]. The top 10% mode was used to focus on the most enriched genes, as it also has a stronger

Fig. 6 | Deletion of a 4-bp noncoding genomic segment containing the rs1882961 orthologous site attenuates salt-induced hypertension in the Dahl salt-sensitive (SS) rat. A Comparative mapping and deletion of a 4-bp rat genomic segment containing the rs1882961 orthologous site. See Supplementary Fig. S11 for additional detail and confirmation of deletion. The image at the top was generated using the UCSC Genome Browser, http://genome.ucsc.edu. The deletion of the 4-bp noncoding genomic segment in the SS rat attenuated salt-induced hypertension (**B**–**G**). **B** Mean arterial pressure (MAP). **C** Systolic blood pressure (SBP). **D** Diastolic blood pressure (DBP). **E** Pulse pressure. **F** Heart rate. **G** Hourly averages of MAP on days 12 to 14 on a 4% NaCl high salt diet. WT wild-type littermate SS rats, Δrs961 SS-Δrs1882961$^{-/-}$ rats. For **B**–**G**, $n = 7$ for WT and 8 for Δrs961. Data are presented as mean ± SEM. #, $p < 0.05$, ##, $p < 0.01$ for WT vs. Δrs961 by two-way RM ANOVA; *, $p < 0.05$ vs. WT by Holm-Sidak test. **H** *Nrip1* expression in the mesentery was lower in SS-Δrs1882961$^{-/-}$ rats compared to WT. In normal salt, $n = 7$ for WT and $n = 9$ for Δrs961; in high salt, $n = 4$ for WT and $n = 5$ for Δrs961. Data are presented as Mean ± SEM. *, p < 0.05, Two-way ANOVA followed by Holm-Sidak test. **I** Vascular smooth muscle sensitivity to nitric oxide (NO) in the 3rd order mesenteric artery was improved in SS-Δrs1882961$^{-/-}$ rats compared to WT. Spermine NONOate, an NO donor. $N = 6$ for WT and 7 for Δrs961 rats. Data are presented as mean ± SEM. ##, $p < 0.001$ for WT vs. Δrs961; *, $p < 0.001$ for 10^{-7} and 10^{-6} M and $p = 0.019$ for 10^{-5} M; two-way RM ANOVA, followed by Holm-Sidak test.

ability to identify associations and aligns more closely with other gene-trait association methods[64]. Significance was determined using a false discovery rate (FDR) of <0.05.

Integrated data analysis

GWAS summary statistics for arteriole-related traits were downloaded from the GWAS Catalog (https://www.ebi.ac.uk/gwas/), including systolic BP, diastolic BP, pulse pressure, essential hypertension, stroke, peripheral arterial disease, diabetic nephropathy, and diabetic retinopathy. Only SNPs with a *p*-value < 5e-8 were retained for further analysis. To assess whether the percentage of SNPs covered by Micro-C or pan-promoter Capture Micro-C in arterioles and EDAs was significantly higher in arteriolar traits, we selected traits not directly or primarily related to the arteriole and calculated their SNP coverage percentages. These traits included birth weight, bone density, breast cancer, colorectal cancer, Alzheimer's disease, Parkinson's disease, multiple sclerosis, rheumatoid arthritis, asthma, psoriasis, and chronic obstructive pulmonary disease. A one-sided binomial test was applied to compare SNP coverage for each arteriolar trait against the average percentage across non-arteriole-relevant traits.

The ClusterProfiler R package (v4.6.2) was used for pathway enrichment analysis on genes associated with arteriole-related SNPs through chromatin interactions captured by pan-promoter Capture Micro-C[65]. Low-abundance genes, defined as those with an average FPKM value less than 0.1 in the bulk RNA-seq data, were excluded from the analysis.

Following the same pipeline as before, SNP regulatory annotation was performed using Ensembl annotation[14]. The coverage of SNPs in each regulatory category by promoter Capture Micro-C was calculated separately for promoter bins and distal bins. A Fisher's exact test was applied to assess whether SNPs were enriched in specific regulatory categories based on their bin location.

Visualization was performed using ggplot2[66].

SNP editing in hiPSCs

The generation of isogenic hiPSCs with homozygous low-BP and high-BP alleles for the SNP rs1882961 was achieved using an efficient two-step approach as we described[26]. Briefly, 3 μM each for two synthetic sgRNAs (Synthego) targeting genomic regions flanking rs1882961 (Supplementary Data S16) and 3 μM spCas9-2NLS nuclease protein (Synthego) with Lipofectamine 2000 transfection reagent (Invitrogen) were used to delete a segment of DNA around rs1882961. After 48 hrs of transfection, cells underwent clonal expansion in 96-well plates using Hana Cell Sorter and Single Cell Dispenser (Bio-Techne). Following single cell seeding, single cell clones were further grown for 10-14 days and characterized for the deletion of SNP region using quick extraction of DNA and PCR (Supplementary Data S16). hiPSC clones showing the intended deletion based on quick extraction of DNA and PCR were further characterized for the deletion by PCR and sanger sequencing. hiPSC line with the deletion of the region around rs1882961 was tested for their genetic stability by molecular karyotyping using hPSC Genetic Analysis Kit (STEMCELL). For the second step of 2-step SNP editing, homology dependent knock-in approach was used with a gRNA targeting the junction of rs1882961 region deletion site and ssDNA donor fragment for low-BP rs1882961-C or high-BP rs1882961-T alleles with 100-200 bp long homology arms at the 3′ and 5′ sides of rs1882961 (Supplementary Data S16). The 500 ng ssDNA donor for either the low-BP rs1882961-C or high-BP rs1882961-T alleles, along with 3 μM each for two sgRNAs targeting junction region and 3 μM spCas9-2NLS Nuclease protein, were transfected into the hiPSC line with the selected clone for rs1882961 SNP region deletion from the first step using Lipofectamine 2000 transfection reagent. Single-cell clonal expansion and initial screening to identify isogeneic hiPSC lines were then performed as described in the first step. Isogenic hiPSC lines with the reconstitution of homozygous low-BP or high-BP alleles were selected, confirmed, and assessed for their pluripotency, differentiation potential, and genetic stability by molecular karyotyping using hPSC Genetic Analysis Kit and Giemsa-based karyotyping.

Differentiation of hiPSCs to vascular smooth muscle cells (iVSMCs)

The differentiation was performed as we described[26,67,68]. Briefly, hiPSCs were treated with mTeSR™ plus medium with 10 μM Rock inhibitor Y-27632 (STEMCELL Technologies) for 24 h and then N2B27 medium (Life Technologies) plus 8 μM CHIR99021 (Selleck Chemicals) and 25 ng/ml BMP4 (PeproTech) for 3 days to generate mesoderm cells. For VSMC induction, mesoderm cells were grown with N2B27 medium supplemented with 10 ng/ml PDGF-BB (PeproTech) and 2 ng/ml Activin A (PeproTech) for 2 days, and N2B27 supplemented with 2 ng/ml Activin A and 2 μg/ml Heparin (STEMCELL Technologies) for 5 days. VSMCs were enriched by removing CD144 + cells using CD144 magnetic beads. Enriched VSMC cells were further cultured in N2B27 medium supplemented with 10 ng/ml PDGF-BB, 2 ng/ml Activin A and 1 μM PD032590 (Selleck Chemicals) for 6 days for contractile VSMC formation.

Real-time PCR

RNA extraction and quantitative real-time PCR analysis were performed as described[69]. Briefly cells were harvested in Trizol reagent (Life Technologies) for total RNA isolation. Approximately 1 μg of total RNA was converted to cDNA using random hexamer primers and RevertAid First Strand cDNA Synthesis Kit (Thermo Scientific). Quantitative PCR (qPCR) was performed on QuantStudio6 Real-Time PCR System (Applied Biosystems) using SYBR Green Master Mix (Applied Biosystems) and primers for neighboring genes. Primer sequences are shown in Supplementary Data S16. Expression levels of mRNAs were normalized to the endogenous control 18S using ΔΔCt method. Statistical analyses were performed utilizing GraphPad Prism 9 (Domatics).

Region-capture Micro-C and data analysis

The assay and data analysis were performed as described with some modifications[26,28,70]. Briefly, Dovetail® Micro-C kit was used to create Micro-C libraries following manufacturer's User Guide. Region capture Micro-C libraries were then generated with reagents from Dovetail® targeted enrichment panels. The panel of 80 bp probes covers the

rs1882961 genomic region and promoters of adjacent protein coding genes. The libraries were sequenced using the Illumina NovaSeq sequencers. Pair-end sequencing reads were cleaned with Trim Galore! to remove adaptor and low-quality reads. We used Juicer to generate.hic file and Juicebox for direct visualization[41].

Animals

The Institutional Animal Care and Use Committee (IACUC) at Medical College of Wisconsin approved all animal related protocols (AUA00000206, AUA00002214). The Dahl salt-sensitive rat (SS/JrHsdMcwi) was used to generate SS-Δrs1882961$^{-/-}$ strain. Because the hiPSCs used in the current study were derived from a female subject, female SS-Δrs1882961$^{-/-}$ rats and wild type littermates were phenotyped accordingly. Animals were housed in a temperature-controlled environment with a 12-h light/dark cycle. Rats had free access to water and a custom AIN-76A purified rodent chow containing 0.4% NaCl (Dyets, Inc) unless otherwise specified.

Generation of SS-Δrs1882961$^{-/-}$ rat

CRISPR/SpCas9 methods were used to delete a noncoding genomic segment in the Dahl salt-sensitive rat (SS/JrHsdMcwi). The LiftOver tool at UCSC Genome Browser placed the non-coding syntenic region to the human rs1882961 at mRatBN7.2 chr11:15,091,368. SpCas9 (QB3 MacroLab, University of California, Berkely) was mixed with a sgRNA targeting the sequence GATGGCCTGCCAGGACAGAGTGG (protospacer adjacent motif underlined and target base in bold) and injected into fertilized SS/JrHsdMcwi strain rat embryos. A founder was identified harboring a 4-bp deletion (mRatBN7.2 chr11:15,091,367-15,091,370 and was backcrossed to the parental strain to establish a breeding colony. This SS-Δrs1882961$^{-/-}$ strain is registered as SS-Del(11p)3Mcwi (RGDID: 407572511). Heterozygous SS-Δrs1882961$^{+/-}$ breeders were maintained on a purified 0.4% NaCl diet AIN-76A (Dyets, Inc).

Telemetry measurement of BP

Continuous measurement of BP in conscious, freely moving female rats ($n = 7$ for WT and 8 for Δrs961) was performed using radiotelemetry as described[71,72]. At 7 weeks of age, rats were anesthetized with a mixture of ketamine (75 mg/kg), xylazine (10 mg/kg), and acepromazine (2.5 mg/kg) intramuscular injection, and a telemetry transmitter (model HD-S10, Data Systems International) was implanted in the right carotid artery to measure arterial blood pressure. After one week of recovery, continuous BP monitoring was started. Following three days of stable baseline BP recording, the diet was switched to an AIN-76A diet containing 4% NaCl (high salt diet) for 14 days. The animal experiments were performed in accordance with the recommendations in the Guide for the Care and Use of Laboratory Animals of the National Institutes of Health. The animal protocols were approved by the Institutional Animal Care and Use Committee at the Medical College of Wisconsin (AUA00000206, AUA00002214).

Vasoreactivity analysis

Vascular function analysis was performed as described[40,73]. Immediately after euthanasia, third order mesenteric arteries from female rats ($n = 6$ for WT and 7 for Δrs961) on an AIN-76A diet containing 4% NaCl for 14 days were dissected and used in the current study. Isolated artery segments were transferred to an organ bath filled with physiological salt solution (PSS) consisting of 119 mM NaCl, 4.7 mM KCl, 1.6 mM $CaCl_2$, 0.03 mM EDTA, 1.17 mM $MgSO_4$, 24 mM $NaHCO_3$, 1.18 mM KH_2PO_4, and 5 mM glucose and mounted between two glass cannulas in a culture myograph chamber (DMT, 204CM). The myograph chamber was transferred to a stage of an inverted microscope attached to a video camera, video monitor, and video-measuring device (model VIA-100; Boeckeler). Arterioles were in PSS buffer bubbled with a gas mixture of 21% O_2-5% CO_2-74% N_2 at 37 °C. The arteriole was allowed to equilibrate at an intraluminal pressure of 30 mmHg supplied by a reservoir system for 30 min and followed by 60 mmHg for another 30 min. After equilibration, U46619 (Catalog No. 16450, Cayman Chemical) was used to pre-constrict the arteriole to 50% to 70% of maximum diameter, followed by administration of 0.1 nM -10 μM spermine NONOate (Catalog No. 82150, Cayman Chemical), a nitric oxide (NO) donor, to construct cumulative concentration-response curves. Vasodilatory response to NONOate is reported as % of maximum dilation, which was defined as (vessel diameter − pre-constricted diameter)/(maximum diameter − pre-constricted diameter), where maximum diameter was the resting diameter or the diameter following the addition of papaverine, whichever was greater.

Data availability

Original and processed omic data are available at Gene Expression Omnibus (GEO) at NCBI with the following accession numbers: Micro-C, GSE288689; promoter-capture Micro-C, GSE288690; RNA-seq, GSE288692; RRBS, GSE288693; and snRNA-seq, GSE288694. Source Data for box plots, bar charts, dot plots, and line graphs are provided with this paper.

Code availability

Code used for omic data processing and analysis is available at https://github.com/yliuphys/epigenomic_landscape_human_arterioles (DOI 5281/zenodo.15335078).

References

1. Rahman, M. & Siddik, A. B. Anatomy, Arterioles. In *StatPearls*. StatPearls Publishing (2023).
2. Martinez-Lemus, L. A. The dynamic structure of arterioles. *Basic Clin. Pharm. Toxicol.* **110**, 5–11 (2012).
3. Tykocki, N. R., Boerman, E. M. & Jackson, W. F. Smooth muscle ion channels and regulation of vascular tone in resistance arteries and arterioles. *Compr. Physiol.* **7**, 485–581 (2017).
4. Kato, M. & Natarajan, R. Diabetic nephropathy–emerging epigenetic mechanisms. *Nat. Rev. Nephrol.* **10**, 517–530 (2014).
5. Touyz, R. M., Montezano, A. C., Rios, F., Widlansky, M. E. & Liang, M. Redox stress defines the small artery vasculopathy of hypertension: how do we bridge the bench-to-bedside gap?. *Circ. Res.* **120**, 1721–1723 (2017).
6. Wong, T. Y., Cheung, C. M., Larsen, M., Sharma, S. & Simó, R. Diabetic retinopathy. *Nat. Rev. Dis. Prim.* **2**, 16012 (2016).
7. Consortium, E. P. et al. Expanded encyclopaedias of DNA elements in the human and mouse genomes. *Nature* **583**, 699–710 (2020).
8. Consortium, G. T. The GTEx Consortium atlas of genetic regulatory effects across human tissues. *Science* **369**, 1318–1330 (2020).
9. Lind, L., Berglund, L., Larsson, A. & Sundstrom, J. Endothelial function in resistance and conduit arteries and 5-year risk of cardiovascular disease. *Circulation* **123**, 1545–1551 (2011).
10. Archer, S. L. et al. Differential distribution of electrophysiologically distinct myocytes in conduit and resistance arteries determines their response to nitric oxide and hypoxia. *Circ. Res.* **78**, 431–442 (1996).
11. Pirruccello, J. P. et al. Deep learning enables genetic analysis of the human thoracic aorta. *Nat. Genet.* **54**, 40–51 (2022).
12. Liu, P. et al. Role of DNA de novo (de)methylation in the kidney in salt-induced hypertension. *Hypertension* **72**, 1160–1171 (2018).
13. Kidambi, S. et al. Dietary sodium restriction results in tissue-specific changes in DNA methylation in humans. *Hypertension* **78**, 434–446 (2021).
14. Martin, F. J. et al. Ensembl 2023. *Nucleic Acids Res.* **51**, D933–D941 (2023).
15. Zerbino, D. R., Wilder, S. P., Johnson, N., Juettemann, T. & Flicek, P. R. The ensembl regulatory build. *Genome Biol.* **16**, 56 (2015).

16. Birdsey, G. M. et al. The endothelial transcription factor ERG promotes vascular stability and growth through Wnt/beta-catenin signaling. *Dev. Cell* **32**, 82–96 (2015).
17. Birdsey, G. M. et al. Transcription factor Erg regulates angiogenesis and endothelial apoptosis through VE-cadherin. *Blood* **111**, 3498–3506 (2008).
18. Guadall, A. et al. Fibulin-5 is up-regulated by hypoxia in endothelial cells through a hypoxia-inducible factor-1 (HIF-1alpha)-dependent mechanism. *J. Biol. Chem.* **286**, 7093–7103 (2011).
19. Carvalheiro, T. et al. Induction of inflammation and fibrosis by semaphorin 4A in systemic sclerosis. *Arthritis Rheumatol.* **71**, 1711–1722 (2019).
20. Peng, H. Y., Gao, W., Chong, F. R., Liu, H. Y. & Zhang, J. I. Semaphorin 4A enhances lung fibrosis through activation of Akt via PlexinD1 receptor. *J. Biosci.* **40**, 855–862 (2015).
21. Yao, L. et al. Temporal control of PDGFRalpha regulates the fibroblast-to-myofibroblast transition in wound healing. *Cell Rep.* **40**, 111192 (2022).
22. Kichaev, G. et al. Leveraging polygenic functional enrichment to improve GWAS power. *Am. J. Hum. Genet.* **104**, 65–75 (2019).
23. Nautiyal, J. Transcriptional coregulator RIP140: an essential regulator of physiology. *J. Mol. Endocrinol.* **58**, R147–r158 (2017).
24. Dekker, J. et al. Spatial and temporal organization of the genome: current state and future aims of the 4D nucleome project. *Mol. Cell* **83**, 2624–2640 (2023).
25. Dekker, J. & Mirny, L. The 3D genome as moderator of chromosomal communication. *Cell* **164**, 1110–1121 (2016).
26. Xue, H. et al. Physiological role and mechanisms of action for a long noncoding haplotype region. *bioRxiv*, https://doi.org/10.1101/2024.05.15.594413 (2024).
27. Mishra, M. K. et al. Comparative and functional genomic resource for mechanistic studies of human blood pressure-associated single nucleotide polymorphisms. *Hypertension* **75**, 859–868 (2020).
28. Goel, V. Y., Huseyin, M. K. & Hansen, A. S. Region capture Micro-C reveals coalescence of enhancers and promoters into nested microcompartments. *Nat. Genet.* **55**, 1048–1056 (2023).
29. Hsieh, T. H. et al. Mapping nucleosome resolution chromosome folding in yeast by Micro-C. *Cell* **162**, 108–119 (2015).
30. Liu, H. et al. DNA methylation atlas of the mouse brain at single-cell resolution. *Nature* **598**, 120–128 (2021).
31. Tan, L., Xing, D., Chang, C. H., Li, H. & Xie, X. S. Three-dimensional genome structures of single diploid human cells. *Science* **361**, 924–928 (2018).
32. Nagano, T. et al. Cell-cycle dynamics of chromosomal organization at single-cell resolution. *Nature* **547**, 61–67 (2017).
33. Khavandi, K. et al. Abnormal remodeling of subcutaneous small arteries is associated with early diastolic impairment in metabolic syndrome. *J. Am. Heart Assoc.* **6**, https://doi.org/10.1161/jaha.116.004603 (2017).
34. Nishijima, Y. et al. Contribution of K(V)1.5 channel to hydrogen peroxide-induced human arteriolar dilation and its modulation by coronary artery disease. *Circ. Res.* **120**, 658–669 (2017).
35. Mohandas, A. et al. Mineralocorticoid exposure and receptor activity modulate microvascular endothelial function in African Americans with and without hypertension. *Vasc. Med.* **20**, 401–408 (2015).
36. Suboc, T. M. et al. Moderate obesity and endothelial dysfunction in humans: influence of gender and systemic inflammation. *Physiol. Rep.* **1**, https://doi.org/10.1002/phy2.58 (2013).
37. Schiffrin, E. L. Remodeling of resistance arteries in essential hypertension and effects of antihypertensive treatment. *Am. J. Hypertens.* **17**, 1192–1200 (2004).
38. Ahn, S. J. et al. Differential effects of obesity on visceral versus subcutaneous adipose arteries: role of shear-activated Kir2.1 and alterations to the glycocalyx. *Am. J. Physiol. Heart Circ. Physiol.* **322**, H156–h166 (2022).
39. Farb, M. G. et al. Arteriolar function in visceral adipose tissue is impaired in human obesity. *Arterioscler Thromb. Vasc. Biol.* **32**, 467–473 (2012).
40. Widlansky, M. E. et al. miR-29 contributes to normal endothelial function and can restore it in cardiometabolic disorders. *EMBO Mol. Med.* **10**, https://doi.org/10.15252/emmm.201708046 (2018).
41. Durand, N. C. et al. Juicer provides a one-click system for analyzing loop-resolution Hi-C experiments. *Cell Syst.* **3**, 95–98 (2016).
42. Roayaei Ardakany, A., Gezer, H. T., Lonardi, S. & Ay, F. Mustache: multi-scale detection of chromatin loops from Hi-C and Micro-C maps using scale-space representation. *Genome Biol.* **21**, 256 (2020).
43. Cairns, J. et al. CHiCAGO: robust detection of DNA looping interactions in Capture Hi-C data. *Genome Biol.* **17**, 127 (2016).
44. Kim, D., Paggi, J. M., Park, C., Bennett, C. & Salzberg, S. L. Graph-based genome alignment and genotyping with HISAT2 and HISAT-genotype. *Nat. Biotechnol.* **37**, 907–915 (2019).
45. Kovaka, S. et al. Transcriptome assembly from long-read RNA-seq alignments with StringTie2. *Genome Biol.* **20**, 278 (2019).
46. Love, M. I., Huber, W. & Anders, S. Moderated estimation of fold change and dispersion for RNA-seq data with DESeq2. *Genome Biol.* **15**, 550 (2014).
47. Liu, Y., Liu, P., Yang, C., Cowley, A. W. Jr. & Liang, M. Base-resolution maps of 5-methylcytosine and 5-hydroxymethylcytosine in Dahl S rats: effect of salt and genomic sequence. *Hypertension* **63**, 827–838 (2014).
48. Krueger, F. & Andrews, S. R. Bismark: a flexible aligner and methylation caller for Bisulfite-Seq applications. *Bioinformatics* **27**, 1571–1572 (2011).
49. Juhling, F. et al. metilene: fast and sensitive calling of differentially methylated regions from bisulfite sequencing data. *Genome Res.* **26**, 256–262 (2016).
50. McGinnis, C. S., Murrow, L. M. & Gartner, Z. J. DoubletFinder: doublet detection in single-cell RNA sequencing data using artificial nearest neighbors. *Cell Syst.* **8**, 329–337.e324 (2019).
51. Hao, Y. et al. Integrated analysis of multimodal single-cell data. *Cell* **184**, 3573–3587.e3529 (2021).
52. Zappia, L. & Oshlack, A. Clustering trees: a visualization for evaluating clusterings at multiple resolutions. *Gigascience* **7**, https://doi.org/10.1093/gigascience/giy083 (2018).
53. Hu, C. et al. CellMarker 2.0: an updated database of manually curated cell markers in human/mouse and web tools based on scRNA-seq data. *Nucleic Acids Res.* **51**, D870–D876 (2023).
54. Franzen, O., Gan, L. M. & Bjorkegren, J. L. M. PanglaoDB: a web server for exploration of mouse and human single-cell RNA sequencing data. *Database* **2019**, https://doi.org/10.1093/database/baz046(2019).
55. Keaton, J. M. et al. Genome-wide analysis in over 1 million individuals of European ancestry yields improved polygenic risk scores for blood pressure traits. *Nat. Genet*, https://doi.org/10.1038/s41588-024-01714-w (2024).
56. Surendran, P. et al. Discovery of rare variants associated with blood pressure regulation through meta-analysis of 1.3 million individuals. *Nat. Genet.* **52**, 1314–1332 (2020).
57. Wojcik, G. L. et al. Genetic analyses of diverse populations improves discovery for complex traits. *Nature* **570**, 514–518 (2019).
58. Malik, R. et al. Multiancestry genome-wide association study of 520,000 subjects identifies 32 loci associated with stroke and stroke subtypes. *Nat. Genet.* **50**, 524–537 (2018).
59. Mishra, A. et al. Stroke genetics informs drug discovery and risk prediction across ancestries. *Nature* **611**, 115–123 (2022).
60. Sakaue, S. et al. A cross-population atlas of genetic associations for 220 human phenotypes. *Nat. Genet.* **53**, 1415–1424 (2021).

61. Zhou, W. et al. Efficiently controlling for case-control imbalance and sample relatedness in large-scale genetic association studies. *Nat. Genet.* **50**, 1335–1341 (2018).
62. Backman, J. D. et al. Exome sequencing and analysis of 454,787 UK Biobank participants. *Nature* **599**, 628–634 (2021).
63. Skene, N. G. et al. Genetic identification of brain cell types underlying schizophrenia. *Nat. Genet.* **50**, 825–833 (2018).
64. Olislagers, M., Rademaker, K., Adan, R. A. H., Lin, B. D. & Luykx, J. J. Comprehensive analyses of RNA-seq and genome-wide data point to enrichment of neuronal cell type subsets in neuropsychiatric disorders. *Mol. Psychiatry* **27**, 947–955 (2022).
65. Yu, G., Wang, L. G., Han, Y. & He, Q. Y. clusterProfiler: an R package for comparing biological themes among gene clusters. *OMICS*. **16**, 284–287 (2012).
66. Wickham, H. *ggplot2: Elegant Graphics for Data Analysis* (Springer-Verlag, 2016).
67. Liu, Y. et al. Robustness of single-cell RNA-seq for identifying differentially expressed genes. *BMC Genomics* **24**, 371 (2023).
68. Pandey, R. et al. Proteomic profiles of human arterioles isolated from fresh adipose tissue or following overnight storage. *Lab Invest.* **104**, 102036 (2024).
69. Cheng, Y. et al. Endogenous miR-204 protects the kidney against chronic injury in hypertension and diabetes. *J. Am. Soc. Nephrol.* **31**, 1539–1554 (2020).
70. Hamley, J. C., Li, H. P., Denny, N., Downes, D. & Davies, J. O. J. Determining chromatin architecture with Micro Capture-C. *Nat. Protoc.* **18**, 1687–1711 (2023).
71. Xue, H. et al. Fumarase overexpression abolishes hypertension attributable to endothelial NO synthase haploinsufficiency in Dahl salt-sensitive rats. *Hypertension* **74**, 313–322 (2019).
72. Tian, Z. M. et al. Renal regional proteomes in young Dahl salt-sensitive rats. *Hypertension* **51**, 899–904 (2008).
73. Wang, J. et al. Acute exposure to low glucose rapidly induces endothelial dysfunction and mitochondrial oxidative stress: role for AMP kinase. *Arterioscler. Thromb. Vasc. Biol.* **32**, 712–720 (2012).

Acknowledgements

This work was supported by National Institutes of Health grants HL149620 (M.L.), DK129964 (M.L.), HL121233 (M.L.) and HL173778 (M.E.W. and M.L.).

Author contributions

Y.L. led omics assays and performed data analysis. R.P. performed hiPSC and molecular experiments. Q.Q. developed data analysis strategies and analyzed and integrated data. P.L. analyzed data. H.X. performed animal experiments. J.W. collected human arterioles. B.T. contributed to omics assays. R.Y. contributed to human arteriole collection. K.U. contributed to animal experiments. M.G. contributed to the development of the mutant rat. C.Y. contributed to human arteriole collection. M.K.M. contributed to hiPSC experiments. A.S.G., A.W.C., S.R. and A.M.G. contributed to study design and data interpretation. A.M.G. led the development of the mutant rat. M.E.W. led the collection of human arterioles and contributed to study conception and design. M.L. conceived and designed the study. Q.Q., Y.L., R.P., P.L., H.X. and M.L. drafted the manuscript. All authors edited and approved the manuscript.

Competing interests

The authors declare no competing interests.

Additional information

Supplementary information The online version contains supplementary material available at https://doi.org/10.1038/s41467-025-61656-7.

Correspondence and requests for materials should be addressed to Mingyu Liang.

Peer review information *Nature Communications* thanks Rhian Touyz and the other, anonymous, reviewer(s) for their contribution to the peer review of this work. A peer review file is available.